Atomistic simulations show how changes in the backbone chirality of peptides can control the formation of coacervate versus precipitate phases.

p*L*K+p*L*E

Potential Steric
Repulsion

L-C$_a$ Carbon

p*L*K+p(*D*,*L*)E

Change in Chirality

Soft Matter
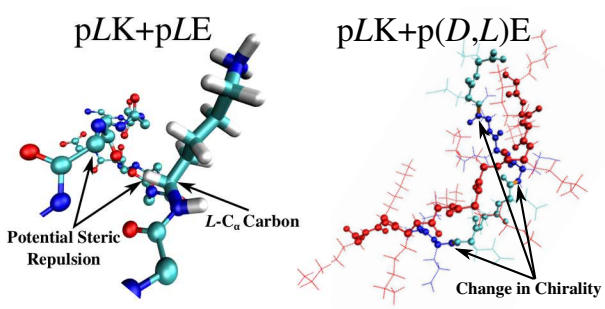
A Molecular View of the Role of Chirality in Charge-driven Polypeptide Complexation

K.Q. Hoffmann,[a] S.L. Perry,[ab] L. Leon,[ac] D. Priftis,[a] M. Tirrell[ac] and J.J. de Pablo[*ac]

Polyelectrolyte molecules of opposite charge are known to form stable complexes in solution. Depending on the system conditions, such complexes can be solid or liquid. The latter are known as complex coacervates, and they appear as a second liquid phase in equilibrium with a polymer-dilute aqueous phase. This work considers the complexation between poly(glutamic acid) and poly(lysine), which is of particular interest because it enables examination of the role of chirality in ionic complexation, without changes to the overall chemical composition. Systematic atomic-level simulations are carried out for chains of poly(glutamic acid) and poly(lysine) with varying combinations of chirality along the backbone. Achiral chains form unstructured complexes. In contrast, homochiral chains lead to formation of stable β-sheets between molecules of opposite charge, and experiments indicate that β-sheet formation is correlated with the formation of solid precipitates. Changes in chirality along the peptide backbone are found to cause "kinks" in the β-sheets. These are energetically unfavorable and result in irregular structures that are more difficult to pack together. Taken together, these results provide new insights that may be of use for the development of simple yet strong bioinspired materials consisting of β-rich domains and amorphous regions.

Introduction

Polyelectrolyte molecules of opposite charge experience strong electrostatic interactions, whose range and magnitude can be manipulated through the addition of salt. Under some conditions, aqueous solutions of polyelectrolytes can lead to the phenomenon of complex coacervation, in which the system undergoes a phase transition into a polymer-dilute and a polymer-rich phase. Coacervates exhibit a small surface tension,[1–3] which has enabled a wide range of applications in the food,[4] cosmetics, and pharmaceutical industries. Coacervates can be formed using synthetic polymers,[5] peptides,[6] DNA,[7] and other biologically degradable components. These viscous, polymer-rich phases can be formed as droplets in microemulsions,[1,6] and engineered for applications in catalysis of reactions and biological mechanisms,[8] gene delivery,[9] encapsulation,[5] and other biological uses.[10]
Complex coacervation should be distinguished from precipitation.[11] Past work has shown that, depending on the experimental conditions, precipitation can also occur, where solid, irregular, polymer-rich masses appear.[6,12] Coacervate phases may contain from 25 to 90% water.[13,14] In contrast, precipitates contain much less water.[12] Whether a coacervate,

precipitate, or only a single phase appears depends on the balance of multiple competing forces. Past studies from several research groups, including our own, have rationalized the interfacial tension and phase behavior of coacervates in terms of the Voorn-Overbeek theory, which predicts that chain length,[13,15] low temperature, and intermediate salt concentrations promote coacervate formation.[14] Low salt concentrations promote precipitation, whereas high salt concentrations tend to inhibit to phase separation.[6] More generally, electrostatic interactions can be tuned by pH,[16] the charge density of the polymers,[17] ionic strength,[18] the type of ions,[19] and stoichiometry.[14] By adjusting these parameters, one can turn on or off the formation of microphases, control their size and density,[20] or change the interfacial tension between the two phases.[2]
The formation of complex coacervates from charged peptides such as poly(lysine hydrochloride) (PLys) and poly(glutamic acid sodium salt) (PGlu)[14] offers additional tunable parameters. Unlike most other polymers used in the past for studies of coacervation, polypeptides can form secondary structures between chains. In particular, hydrogen bonds between the backbones of the chains can lead to β-sheet formation where the mobility of the chains is reduced and longer-range aggregates or structures are formed. Most naturally occurring proteins or

polypeptides are composed of predominantly *L*-amino acids: the substitution of *D*-amino acids is found to inhibit the formation of secondary structure[21,22] and can be used to tune the stiffness and other properties of synthetic hydrogels.[23] These observations suggest that, by only changing the chirality of certain C$_\alpha$ atoms and thereby the secondary structure, one can tune properties such as viscosity, water content, and size while leaving other parameters such as chain length, salt concentration, and pH unaltered. Indeed, in recent experiments Perry *et al*.,[24] have discovered that achiral polypeptides form stable coacervates, whereas homochiral peptides form solid precipitates, rich in β-sheet content. These new observations are intriguing, and the underlying molecular forces responsible for the role of chirality in polyelectrolyte complexation are not well understood. Hydrogen bonding, salt bridge formation, coulombic interactions, and solvation by water, could all contribute to the formation of solid precipitates versus liquid coacervates.[19,25–27]

Motivated by the findings of Perry *et al*.,[24] in this first theoretical investigation of the influence of chirality in polyelectrolyte complexation, we consider polypeptide-based coacervation between poly(lysine) and poly(glutamic acid) using fully atomistic models. First, the interaction between homochiral poly(*L*-lysine) and an achiral poly(*D,L*-glutamic acid) system is examined using replica exchange with solute scaling.[28] The low energy conformations are analyzed to learn how chirality affects backbone hydrogen bonding, secondary structure formation, and other properties. Key trends and metastable states are then identified for pairs of short peptides with different chirality sequences of the poly(*D,L*-glutamic acid) chain. By examining these, we provide new insight into conditions that may lead to formation of liquid coacervates versus solid precipitates. The formation of energetically stable β-strands between pairs of peptides is then shown to correlate with recent experiments[24] on the formation of precipitates rich in β-sheet character.

Methods

Past theoretical or computational studies of coacervation have relied on various levels of theory[1] and coarse-grained representations of the molecules.[29] In order to examine the role of chirality, however, one has little choice but to rely on detailed atomistic representations of the molecules. Experiments suggest that relatively small polypeptides can lead to coacervation.[7] We therefore consider poly(glutamic acid) and poly(lysine) chains of 10 residues each which, as described in this manuscript, are sufficiently long to explain many of the experimentally observed features of chiral or achiral complexation.

Molecular Simulations

Molecular simulations were performed in order to identify important trends in secondary structure formation. While standard molecular dynamics (MD) simulations are unable to sample conformational space exhaustively, they provide useful

qualitative information and can identify important metastable states. They also provide information on the dynamics of system and the relative time scales for various modes of assembly. MD simulations were initially run for a series of pairs of peptides. A 10-residue poly(*L*-lysine) molecule was included in all of the simulations. For the negatively-charged chain, the length of consecutive *L*-glutamic acids in the center of the chain was varied. A list of the PGlu sequences considered here is given in Table 1. The first sequence was chosen by shuffling a sequence of 5 *L*- and 5 *D*-amino acids; for sequences A4 and A5, the chirality of the backbone C$_\alpha$ atoms was shuffled until a sequence where 4 and 5 consecutive, non-terminal *L*-amino acids was found. The longer sequences were generated by putting all of the *L*-amino acids in the middle of the chain and the *D*-amino acids on the ends. The side chains were fully charged and the N-terminus and C-terminus consisted of a charged NH_3^+ and a charged COO^- group, respectively. The chains were initialized into a β-sheet like conformation, where the φ and ψ angles were -113° and 120°, respectively. One poly(glutamic acid) chain and one poly(lysine) chain were placed perpendicularly to each other, about 1 nm apart, in a 6 nm dodecahedral box. The systems were solvated with 4889 TIP3P[30] water molecules and 16 Na$^+$ and Cl$^-$ ions in order to reach a concentration of approximately 175 mM, which was chosen because it is in the experimentally relevant coacervate phase region and is close to a physiological salt concentration.

Table 1. List of sequences of PGlu simulated using MD simulations. The initial letter denotes whether a sequence is achiral (A) or homochiral (*L* or *D*).

Name Used	PGlu Chiral Sequence
A3	*LLDDDLLLDD*
A4	*DDLLLLDDDL*
A5	*DDDLLLLLDD*
A6	*DDLLLLLLDD*
A7	*DLLLLLLLDD*
A8	*DLLLLLLLLD*
L	*LLLLLLLLLL*

If a number follows the letter, it denotes the longest homochiral stretch of amino acids in the sequence. For example, the longest consecutive stretch of *L* in A4 is four amino acids long. These peptides were all paired with a single 10-residue poly(*L*-lysine) peptide.

The CHARMM22* force field[31,32] was chosen because it is believed to provide an adequate description of secondary structure.[32,33] In order to simulate *D*-glutamic acid, the φ and ψ dihedral potentials were modified to reflect the change in steric interactions from *L* to *D* chirality embedded in the dihedral parameters. A new atom type was created for *D*-amino acids, which is identical to the old C$_\alpha$ atom type used (the CT1 atom type) with respect to all properties and interactions with other atoms, except for the φ and ψ dihedral potentials. Because the *D*-amino acids are a mirror image to the *L*-amino acids, the

potentials for the φ and ψ dihedrals of the residues with *D* chirality were changed as follows: $f_D(\varphi) = f_L(-\varphi)$ and $g_D(\psi) = g_L(-\psi)$.

In addition, the standard CHARMM22* ion parameters were not used in this work because the balance between protein, water, and ionic interactions is critical to coacervation. These parameters lead to artifacts such as crystallization at NaCl concentrations of less than 2M.[34] Instead, the recently optimized ion parameters from Joung *et al.*,[35] were employed. Because these parameters are limited to the TIP3P, TIP4P-EW, and SPC/E water models, the TIP3P water model was chosen as it is most similar to the water model optimized for CHARMM22* (TIPS3P) and is almost indistinguishable in performance.[31]

The Gromacs 4.6.3 simulation package[36] was used for all MD simulations. An energy minimization was first performed for 500 steps before constraints were added to the bonds. The energy minimization was continued for another 10,000 steps or until the change in energy was < 100 kJ, using the steepest descent algorithm. An NVT simulation was then performed for 100 ps at 298 K and 1 bar. Production MD runs were then started and run for at least 1 μs. The Nose-Hoover[30] and Parrinello-Rahman[37] algorithms were used to control the temperature and pressure, respectively. A step size of 2 fs was used for both the NVT and NPT simulations. The Particle Mesh Ewald method (PME)[38] with a cut-off of 0.9 nm and a Fourier spacing of 0.33 nm was used to handle electrostatic interactions. Rigid bonds to hydrogen atoms were constrained using the LINCS algorithm.[39]

REST2 Simulations

In order to achieve better sampling of phase space than that provided by standard MD, we also pursued Replica Exchange with Solute Scaling molecular dynamics simulations.[28] Note that the high charge density along the side chains and terminal groups results in the formation of a large number of salt bridges. These salt bridges are highly stable, and contribute 1-5 kJ/mol of energy per bridge to the system.[20] For the solutions considered here, at 298 K (kT = 2.48 kJ/mol), the formation of several of these salt bridges leads to long-lived structures. Peptide-peptide hydrogen bonds are also stable, leading to additional sampling concerns.[40]

Parallel tempering, or replica exchange,[41–44] is used extensively in the protein and materials simulation literature to simulate multiple replicas simultaneously at various temperatures. Replicas at high temperatures exhibit faster relaxation, thereby accelerating exploration of conformations that would be difficult to access in individual, low-temperature simulations. When combined with umbrella sampling, this technique was used to efficiently sample secondary structures of amylin in the replica exchange with umbrella sampling method.[45] The so-called Replica Exchange with Solute Tempering method[46] (REST) uses a variant of parallel tempering in which the system is divided into two parts. The goal is to eliminate water-water interactions, therefore greatly reducing the number of degrees of freedom and accelerating the relaxation of the actual solute

of interest. Replica exchange with solute scaling (REST2)[28] improves upon this technique by better exchanging boxes with different peptide-solute interactions. REST2 was used to determine the low free energy states of two peptide pairs: homochiral PLys and homochiral PGlu (p*L*K+p*L*E), and homochiral PLys and achiral PGlu (p*L*K+p(*D,L*)E). Sixteen replicas, varying in the equivalent temperature of the protein from 298 to 600 K were used in our simulations. The initial conformation of each state was taken from the MD simulation of the peptide pair at 100 ns. The 6 nm radius dodecahedral box was used, and the initial temperatures were chosen geometrically. These temperatures were optimized every 50 ns using the flux-optimized scheme by Katzgraber *et al.*,[47] Both systems were run for 500 ns, at which point the p*L*K+p(*D,L*)E pair reached convergence. The p*L*K+p*L*E was run for an additional 500 ns (for a total of 1 μs) to achieve convergence. The Gromacs implementation by Bussi *et al.*,[48] was compiled for Plumed 2.02[49] and Gromacs 4.6.5.[36] A custom Python script was used to scale protein energies of topology files for the CHARMM22* force field, instead of the script provided in the REST2 distribution.

Analysis

The secondary structures were determined using the DSSP criteria.[50] The center-of-mass and radius of gyration for the peptides and their main chains were determined using the built-in Gromacs utilities.[36] The number of hydrogen-bonds versus time was also calculated using the Gromacs utility. A hydrogen bond is registered if the distance between the donor and acceptor groups is smaller than 0.35 nm and the angle between the hydrogen, donor, and acceptor is smaller than 30°. The structures were visualized using VMD 1.9.1.[51] Further analysis was performed using custom python scripts. The REST2 simulations of p*L*K+p(*D,L*)E quickly reached equilibrium; the properties of these simulations were therefore averaged over the first 500 ns. However, the p*L*K+p*L*E system needed more time to converge. Each replica was run for a total of 1000 ns. The last 500 ns were then used for analysis.

Experiments

A more extensive account of the experimental system considered here is provided in Ref. 24. Here we merely provide an account of essential aspects of those experiments. Poly(glutamic acid) (pE) and poly(lysine) (pK) were combined in stoichiometric quantities to obtain overall concentrations of 1 mM. The pH was kept at 7.0, where approximately all residues are charged. pE was added first to a solution of salt, followed by pK. After each addition, vortexing was performed immediately in order to mix the samples. The overall concentration of salt was 100 mM NaCl. Images were taken within 1 hour of preparation using brightfield microscopy with a Leica DMI6000 B. The average length of the peptides used was 100 residues. This was performed with both homochiral p*L*E and achiral p(*D,L*)E. D_2O was used to facilitate FTIR measurements.

Analysis of the secondary structure of the various solid precipitates and liquid coacervates was performed using a transmission FTIR microscope.[52] The instrument used was a Bruker Vertex 70 FTIR microscope spectrophotometer with a MCT detector. A 0.45NA condenser and a 15X Cassegrain-type IR objective was used. The sample was prepared in D_2O and centrifuged prior to use. The sample was held between two 1-mm thick CaF_2 windows with a 50 μm PTFE spacer. The sample chamber was purged with N_2. Scans were collected from $4000 – 600$ cm^{-1} at a spectral resolution of 2 cm^{-1}. The microscopic setup enabled direct sample visualization and targeting. A background in the same cell, away from the aggregated solid precipitates or liquid coacervate droplets was used. The location of individual peaks was determined using non-linear least squares fitting of Gaussian peaks to the features of the spectrum.

Results

REST2 Simulations

Two pairs of peptides were selected to explore the low free energy states of poly(glutamic acid) and poly(lysine) using replica exchange with solute scaling (REST2). Homochiral poly(*L*-lysine) and homochiral poly(*L*-glutamic acid) (p*L*K+p*L*E) provide a control with no changes in chirality (L strand). In contrast, the A3 strand from Table 1, homochiral poly(*L*-lysine) and achiral poly(*D,L*-glutamic acid), or p*L*K+p(*D,L*)E, contains both *L*- and *D*-amino acids. These two pairs serve to demonstrate the role of chirality in determining secondary structure.

For the achiral p*L*K+p(*D,L*)E system, a diverse set of disordered structures exist, where the chains can be extended or compact, and in either tighter contact with the oppositely charged chain or further apart. The secondary structure of each residue versus time is shown in Figure 1, along with some of the conformations sampled. PGlu is shown in blue while PLys is shown in red. Many β-sheet structures, both parallel and anti-parallel, are formed between the three consecutive residues of PGlu and the PLys strand as seen in conformations A and B. These β-sheets are formed primarily between the *L*-amino acids on residues 6-8 of the PGlu with the PLys chain. Occasionally, a bent β-sheet forms along the entire PGlu backbone with PLys, for example in conformation E. However, this structure is short-lived and should be contrasted with the more standard β-sheets found in the p*L*K+p*L*E system.

When both strands are homochiral *L* (p*L*K+p*L*E), conformations composed primarily of β-sheets appear very quickly, within 10 ns of time. Several variants of β-sheets are observed on time scales leading to about 500 ns, including aligned and off-center parallel β-sheets (conformation F). Similarly, we see anti-parallel β-sheets in both shifted (conformation H) and matched arrangements (conformation I). The end groups have more entropic freedom and therefore tend to adopt a non β-sheet conformations more frequently than the center of the strands (for example the C-terminus of PGlu and

N-terminus of PLys in conformation J). In the last 500 ns of the simulation, the vast majority of the structures exhibit well defined anti-parallel β-sheets. The β-sheets at the end of the simulations, when it is converged, tend to favour a somewhat twisted conformation, as is typical for β-sheets.

These differences, which are easily identified visually, are confirmed when the average secondary structure versus time is examined in more detail. Figure 2 shows the overall average using thick, solid lines, and the local, running average over a 10 ns interval, using thin, dotted lines. The p*L*K+p(*D,L*)E pair forms a predominantly unstructured coil (61%), with a significant amount of strand (β-sheet or β-bridge) content (24%), and about 10% bend and 4% turn. In contrast, the p*L*K+p*L*E pair contains on average 62% β-sheet, and 37% random coil. The fraction of peptides in a given secondary structure converges after approximately 100 and 600 ns, respectively, and remains relatively unchanged over the last 500 ns of the simulations. On this basis, we conservatively average over the last 500 ns of each simulation to evaluate the properties of the system.

When these overall fractions of secondary structure are broken down by residue, as shown in the Supplementary Information Figure S1, it is apparent that β-sheets are typically formed across the homochiral L segments of the peptides. In the p*L*K+p*L*E system, the six residues in the center of the poly(glutamic acid) and poly(lysine) are involved in a strand (β-sheet or β-bridge) at least 80% of the time. When the chirality is changed as in p*L*K+p(*D,L*)E, strand formation continues to occur throughout the homochiral poly(*L*-lysine). However in the case of poly(glutamic acid), residues 6-8 which form a three residue homochiral *L* segment, are the location of the vast majority of strand confirmations. At the change to *D* residues, the fraction of time each residue spends as a strand drops.

This difference in secondary structure is correlated with changes in other properties such as the center-of-mass distance (COM) between the peptide backbones, hydrogen bonding, and radius of gyration. The COM distance predicted between the PGlu and PLys main chains (Figure 3) remains near 2.9 Å for p*L*K+p*L*E. For p*L*K+p(*D,L*)E, meanwhile, the complex adopts many more structures where the main chains are not joined by hydrogen bonds and remain further apart, resulting in a larger COM distance of 5.7 Å. In addition, the formation of more β-sheets in p*L*K+p*L*E indicates the formation of additional hydrogen bonds between the main chains, as confirmed in Figure 4. On average, 3.5 hydrogen bonds are formed between the main chains of p*L*K+p(*D,L*)E, while for p*L*K+p*L*E, this average more than doubles, to 7.3. A large number of the hydrogen bonds between the backbones are with residues formerly hydrogen bonded to water: the average number of peptide-water hydrogen bonds drops from 107.4 in p*L*K+p(*D,L*)E to 101.5 in p*L*K+p*L*E.

The radius of gyration of the main chain reflects the trends seen in the MD simulations, as shown in Figure 5: chains with more β-sheet character form more extended chains. Both the PLys and PGlu chains of p*L*K+p*L*E are relatively extended, with the

radius of gyration of the PGlu and PLys main chains at 8.4 Å and 8.3 Å, respectively. In contrast, in the pLK+p(D,L)E system, the pLK chain is more compact, with a radius of gyration of 7.9 Å, while the p(D,L)E chain adopts an even tighter conformation, with a radius of gyration of 6.9 Å. Despite the more compact arrangement of the individual chains, the overall pLK+p(D,L)E system forms a looser complex, as revealed by the relatively large fluctuations of the radius of gyration.

The contact maps shown in Figure 6 show that the pLK+pLE pair favors anti-parallel β-sheets, while the residues of pLK+p(D,L)E interact with a variety of partners, indicating a disordered structure. For pLK+pLE, each residue interacts primarily with the 2-3 residues on the opposite end of the oppositely charged chain. This manifests in a band across the diagonal, indicating a strong preference for interactions with residues on the opposite end of the other chain. In contrast, pLK+p(D,L)E forms more globular structures, lowering the mean distance of many residues not in direct contact. Each residue of poly(glutamic acid) interacts with many different residues throughout the poly(lysine) chain. Therefore, the average distance is relatively uniform across the residues.

The stronger interactions formed between the peptides in the pLK+pLE system are accompanied by differences in the distribution of ions around the peptide when compared to pLK+p(D,L)E. Figure 7 shows the radial distribution functions (rdf) of the ions with PGlu and PLys. The rdf for the main chains and side chains are shown separately. In general, three regions exist: the immediate vicinity of the main chain/side chain, the rest of the polypeptide, and the bulk solution. In the vicinity of the PGlu main chain, the two peaks for Na$^+$ correspond to the carbonyl oxygens in the backbone. The first peak is higher in the pLK+p(D,L)E system than for pLK+pLE. This is likely because the oxygens in the pLK+pLE system are involved in hydrogen bonds. Furthermore, the β-sheets of the pLK+pLE system cause the chains to bind more tightly, making it more difficult for ions to diffuse into the backbone region. Cl$^-$ ions are excluded from the region around the main chains. Their large size (in comparison to Na$^+$) makes it even more difficult to come in close contact with the backbone. Little difference in seen for the Na$^+$ ions with respect to the PLys chains between the pLK+pLE and pLK+p(D,L)E systems. There is a slight increase in the first peak, corresponding to an increase of ions near the oppositely charged strand in PGlu. Cl$^-$ is largely excluded from the PLys main chain, though a slight increase is observed for pLK+p(D,L)E compared to pLK+pLE. Cl$^-$ is largely excluded from the PGlu chain, though it returns to the bulk density more quickly in the case of pLK+pLE than for pLK+p(D,L)E. We attribute this to a sharper transition from the peptide region to the bulk solution in pLK+pLE compared to pLK+p(D,L)E. In the homochiral case, the peptides are nearly always matched pair for pair, forming a set of structures with a relatively constant radius of gyration. However, in pLK+p(D,L)E, residues bind to many different residues on the opposite strand as seen in the contact maps in Figure 6. When the pairs are "mismatched," the PGlu can extend further than

when the peptides bind to their native contacts. The exclusion of Cl$^-$ by the PGlu chain in this region results in a slower return to the bulk value in the achiral case.

More drastic differences between pLK+p(D,L)E and pLK+pLE are observed in the ion densities near the side chains. In both systems, Na$^+$ ions are more abundant in the region around the PGlu side chains than in the bulk. However, in pLK+p(D,L)E, Na$^+$ is more often bound to the carboxylic acid of the PGlu side chains compared to pLK+pLE. This suggests that the side chains of pLK+p(D,L)E are more accessible to Na$^+$ compared to pLK+p(D,L)E. The negative carboxylate group on the glutamic acid side chain forms many salt bridges with the positive lysine side chain. The achiral system, however, forms fewer salt bridges between the side chains than in the homochiral system. Because the side chains are bound less frequently to each other, they remain exposed to solvent. Furthermore, the charges on the chains are not neutralized as often by the oppositely charged side chains of the other peptide.

In contrast to Na$^+$, Cl$^-$ is mostly excluded from the space around the side chains of both PGlu and PLys. The Cl$^-$ ions interact most strongly with the positive terminus of the PLys side chains. The first peak, corresponding to the binding of Cl$^-$ to the amide group, is roughly equal for pLK+p(D,L)E and pLK+pLE. This suggests that the NH$_3^+$ terminus prefers to bind other atoms, such as the carboxylic acid of PGlu. Na$^+$ ions are much smaller compared to Cl$^-$ ions. The smaller Na$^+$ ions are able to access the carboxylic acid side chains of PGlu. However, the larger Cl$^-$ ions have more difficulty binding to the charged PLys terminus. Cl$^-$ is more prevalent in the achiral system further away compared to the homochiral pair. We attribute this to increased access of the Cl$^-$ ion to the lysine side chains.

When the hydrogen bonds between the peptides are broken down by component, they confirm that the side chains of pLK+p(D,L)E do not form hydrogen bonds with each other as often as in pLK+pLE. Results are shown in Figure 8; on average, a larger number of hydrogen bonds are formed between the side chains in pLK+pLE. Correspondingly, while the number of main chain-main chain H-bonds increases for pLK+pLE, fewer H-bonds are formed between the PGlu main chain and itself and the side chains compared to pLK+p(D,L)E.

MD Simulations of Peptide Pairs

Molecular dynamics simulations were used to observe trends in secondary structure formation as a function of chiral sequence. While REST2 simulations can better explore the conformational space of a system, they are more computationally demanding and do not provide information on the dynamics of assembly. Molecular dynamics simulations on a set of chiral sequences of varying homochirality provide qualitative information about the metastable states and timescales on which the peptides interact.

After 1 µs, all pairs of peptides are able to form some β-sheets, which generally increase in length as the chains contain longer stretches of L-amino acids. Figure 9 shows the secondary structure of pairs A3, A5, A8, and the homochiral L pair as a function of time. The conformations at 0, 400, 700, and 1000 ns

are shown on the right. The remaining pairs are shown in the Supplementary Information Figure S2. The total number of residues in a strand conformation (β-sheet or β-bridge) versus time is given in Figure 10. p*L*K+p*L*E quickly forms a parallel β-sheet after about 100 ns of simulation time. Likewise, the sequence with 8 consecutive *L*-glutamic acid residues (A8) forms a parallel β-sheet. However, the A7 sequence, while forming a number of small β-sheets, does not adopt a β-sheet structure spanning more than a few residues in the first 1 µs: only residues 5 and 6 of PGlu and residues 3 and 4 of PLys have formed a β-sheet. For sequences A4-A6, relatively few β-sheets appear. The A6 sequence forms a small β-sheet segment between residues 3-5 and residues 5-7 of PLys that, while present, never extends during the duration of the simulation. During the last 200 ns of the A5 pair, a more extended β-sheet appears with a kink at the transition from *L*- to *D*-amino acids. The A4 sequence is similar to the A6 sequence, with residues 4-6 of PGlu and 2-4 of PLys transiently forming β-sheets. The A3 sequence samples a range of disordered structures and occasionally forms β-sheets. Residue 6 of PGlu and 3 of PLys form a β-bridge quickly. The β-bridge then dissolves before small parallel β-sheets form between residues 7 and 8 of PGlu and 6 and 7 of PLys near the end of the simulations.

The β-sheets observed in simulations appear primarily between segments with consecutive *L*-glutamic acid residues. Only in sequence A5 does a more extended kinked "β-sheet" form; however it forms at the end of the simulation, making its stability unclear. In general, the β-sheets for sequences A3-A7 appear transiently and often fluctuate into and out of a conformation through the trajectory. These sequences explore many more disordered states than the homochiral L and A8 sequence. The length of β-sheet in the A8 pair grows throughout the course of the simulation, and the homochiral L strand forms an extended β-sheet within the first 200 ns that remains stable for the rest of the 800 ns simulated.

The number of hydrogen bonds between PGlu and PLys, and PGlu and water reflects the trends in secondary structure, as shown in Figure 11. As β-sheets form between the main chains, the corresponding hydrogen bonds between PGlu and PLys also form. Molecules that exhibit extended β-sheets have more hydrogen bonds between the two chains. The number of hydrogen bonds between PGlu and water follow the opposite trend: strands with less β-sheet content have more hydrogen bonds with the water.

The radii of gyration of poly(glutamatic acid) and poly(lysine) are also correlated with β-sheet formation as seen in Figure 11. Structures with the largest β-sheet content are the most extended. The more achiral structures have a smaller radius of gyration, as the poly(glutamatic) and poly(lysine) fold about themselves in order to maximize the number of salt bridges. In general, poly(lysine) is more extended than poly(glutamic acid).

Experiments

Experimental measurements by Perry et al.[24] confirm the general trends observed in simulations. Figure 12, which is

taken from the experimental literature,[24] shows brightfield microscopy images of the two systems in the top panel (two images), while the bottom panel shows results of FTIR measurements. For the p*L*K+p*L*E system, precipitates are formed as seen in the brightfield image. The precipitate sample shows several peaks: at 1642 cm^{-1} indicating a random coil structure, a peak at 1563 cm^{-1} corresponding to the glutamic acid side chain, and two sharper peaks at 1678 cm^{-1} and 1610 cm^{-1} indicating the presence of β-sheet structures. The p*L*K+p(*D,L*)E system however forms spherical coacervate droplets. Only two peaks are seen for this system: the random coil peak at 1646 cm^{-1} and the glutamic acid side chain peak at 1562 cm^{-1}. These findings are in agreement with the simulation results, where achiral peptides disrupt the β-sheets form and instead remain mostly random coil. Instead, the homochiral peptides form β-sheet structures and a precipitate phase.

Discussion

The REST2 simulations show that the chirality of the peptide backbones influences the secondary structures of the two-chain complexes considered here. In the case of p*L*K+p*L*E, over 99% of dimers form a β-sheet. The majority of these β-sheets include the six residues in the center of the chain. There are a number of hydrogen bonds formed between the peptide backbones, serving to stabilize these structures. In contrast, while 63% of the p*L*K+p(*D,L*)E pairs present a β-sheet, these typically extend only between the homochiral L residues 6-8 of PGlu. The rest of the PGlu molecule rarely forms β-sheets, in contrast to the PLys molecule, where most of the chain occasionally forms a β-sheet with these residues.

This increase in β-sheet character for p*L*K+p*L*E compared to p*L*K+p(*D,L*)E is correlated with the radius of gyration of the main chains. Figure 13 shows that for p*L*K+p*L*E and p*L*K+p(*D,L*)E, when the number residues classified as coil is high, the distribution of structures with a radius of gyration is similar for p*L*K+p*L*E and p*L*K+p(*D,L*)E. However, when the structures are mostly classified as β-sheets, the distribution is different in p*L*K+p*L*E compared to p*L*K+p(*D,L*)E. Even when the number of residues in a β-sheet is roughly the same, the conformations of p*L*K+p(*D,L*)E typically have a smaller radius of gyration than in p*L*K+p*L*E. These histograms show that p*L*K+p(*D,L*)E's large β-sheets have a smaller radius of gyration, indicating that the peptides are more globular. This is confirmed visually by conformation E of Figure 1, where the peptides form a kink where the chirality changes. This kink in the backbone results in a smaller radius of gyration and a more bent structure, even when the number of residues in a β-sheet is the same.

This kink is a result of the change in chirality along the backbone. Figure 14 shows the structure of the backbone of p*L*K+p*L*E when the peptides are in an anti-parallel β-sheet conformation. In order to minimize steric repulsions between the side chains, a twist is often seen in anti-parallel β-sheets.[53] For p*L*K+p*L*E, we observe that if the chirality of every other residue is changed from *L* to *D*, the side chains extend into the

opposite peptide's backbone. It is possible for the peptide to avoid these interactions and continue forming a β-sheet, as seen in the case of pLK+p(D,L)E; however, this then introduces a kink in the β-sheet at this residue or the next one. This kink is observed in all three places in pLK+p(D,L)E where the chirality changes.

We propose that when two pairs of pLK+pLE peptides come together, they are able to more readily pack and form inter-peptide hydrogen bonds, facilitating the formation and growth of precipitates. In contrast, peptides with pLK+p(D,L)E can only form kinked and irregular β-sheets, resulting in a less compact packing, more peptide-water hydrogen bonds, and a reduced number of inter-peptide contacts. While the peptides still form strong inter-peptide interactions, they cannot tightly pack, and so remain more accessible to ions and water. This allows the eventual dissolution of the secondary structure and formation of a coacervate phase. The increased access to ions is reflected in the radial distribution functions of the ions around the peptides shown previously in Figure 7.

As alluded to earlier, experiments[24] have shown that while mixes containing a racemic mix of L,D-amino acids form coacervates, if both peptides are homochiral, they instead form precipitates.[24] The corresponding FTIR measurements show that while the complex coacervate phase consists of mostly random coil structures, the precipitate phase exhibits β-sheet formation. Additional circular dichroism measurements further support these results.[24] Interestingly, urea is known to disrupt the backbone hydrogen-bonds associated with secondary structure.[54] While urea has little effect on coacervates phases – in contrast to how a salt with equivalent concentration would, when added to precipitate solutions it causes the precipitates to dissolve and form coacervate like liquids.[24] These experiments are consistent with the results presented in this work, and serve to establish that the chirality of the peptides can be used to change the properties of the peptide rich phase.

The MD simulations highlight several important trends, which help explain why homochiral chains precipitate out of solution while systems with achiral chains form coacervates. In these simulations, a randomly shuffled PGlu chain with five L-glutamic acids and five D-glutamic acids forms a mostly disordered dimer complex with a 10-residue homochiral L PLys chain. In contrast, when both chains are homochiral L, a parallel β-sheet forms within 200 ns, and is stable for time scales approaching a microsecond. This suggests that these peptides quickly form dimers. As the total peptide concentration is typically low, e.g., 0.01-0.20 wt%,[14] the peptides most likely first interact in pairs. In the case of homochiral chains, the chains rapidly adopt a stable β-sheet dimer. Therefore, when larger numbers of chains in these systems interact, they most likely do so first as pairs of β-sheets.

However, the number of consecutive L-glutamic acids is critical to the formation of stable, large β-sheets. The number of L-glutamic acids in the middle of the chain was varied from 4 to 8. In these simulations, only the sequence with 8 consecutive L-amino acids formed a stable β-sheet structure within 1 µs.

While PGlu chains with smaller homochiral segments transiently formed stable β-sheets, these were unable to extend past transitions in chirality. Instead, the rest of peptide remained in a disordered state.

This dependence on the length of the peptides suggests that the fraction of L and D amino acids can be used to tune the properties of the resulting peptide rich phase. By changing the ratio of L to D amino acids, the average maximum length of consecutive L amino acids can be changed. To determine the distribution of the average maximum length of consecutive L-amino acids, 100,000 one hundred residue L/D sequences were generated. The chirality of each residue in the chain was assumed to be independent, and the probability of choosing an L or D amino acid was set to 0.5 and 0.68. The distribution of the maximum length, shown in the Supplementary Information Figure S3, shows that most chains with a 0.68 L-amino acid fraction have at least eight consecutive L-amino acids. In contrast, most chains with a probability of 0.5 have less than eight consecutive L-amino acids. Perry et. al[24] conducted experiments where the ratio of L to D-amino acids was changed from 50% L to 68% L for poly(glutamic acid) chains on average 100 residues long. In this case, the 68% L poly(glutamic acid) chains formed precipitates with the homochiral poly(L-lysine), while the 50% L mixture instead formed a coacervate phase, confirming that this ratio can be used to tune the properties of the peptide rich phase.

Conclusions

Conformations of the pLK+p(D,L)E and pLK+pLE pairs were extensively sampled using replica exchange solute scaling. pLK+pLE peptide pairs formed β-sheets in over 99% of the structure sampled after convergence. These pairs contained many peptide-peptide backbone hydrogen bonds stabilizing this structure. The structures were extended and contained a regular β-sheet structure. In contrast, while pLK+p(D,L)E formed β-sheets between the homochiral poly(L-glutamic acid) segment on residues 6-8 with the homochiral poly(L-lysine), β-sheets typically did not extend past these residues. When longer β-sheets formed, a kinked β-sheet was observed. These structures had smaller radius of gyrations than their homochiral counterpart, indicating that pLK+p(D,L)E adopts a more globular formation.

Increasing the length of the homochiral poly(L-glutamic acid) sections led to the observation of trends in β-sheet content and radius of gyration when molecular dynamics simulations were conducted of the pairs for 1 µs. In all simulations, the peptides quickly formed inter-protein salt-bridges and remained bound at all times. As the homochiral L PGlu section increased, the length of the β-sheets formed also increased. Significant β-sheet formation was found within 200 ns, indicating that peptides can quickly adopt β-sheet conformations stabilized by peptide-peptide hydrogen bonds and salt-bridges between the two strands. Considering that the peptides immediately bind to each other and are stable through the duration of the simulation, we suggest that homochiral peptides interact in larger groups first

as pairs of β-sheets. In contrast, systems with more achiral character only formed β-sheet conformations on the polyglutamic acid chain for amino acids part of the homochiral *L* chain. These peptides were more disordered and globular than the homochiral peptide pairs.

We hypothesize that this more globular, random coil rich pair is unable to pack as well as p*L*K+p*L*E, leading to easier access for ions and water. As a result, a coacervate phase is observed for the p*L*K+p(*D,L*)E system. In contrast, p*L*K+p*L*E dimers form extended, regular β-sheets that are better able to pack. These β-sheets are better able to bond tightly together, resulting in the formation of a precipitate phase.

Acknowledgements

Notes and references

a Institute for Molecular Engineering, University of Chicago, Chicago IL 60637, USA. E-mail: depablo@uchicago.edu.

b Department of Chemical Engineering, University of Massachusetts Amherst, Amherst MA 01003, USA

c Institute for Molecular Engineering, Argonne National Laboratory, Argonne, IL70439, USA

1   J. Qin, D. Priftis, R. Farina, S. L. Perry, L. Leon, J. Whitmer, K. Hoffmann, M. Tirrell and J. J. de Pablo, *ACS Macro Lett.*, 2014, 565–568.

2   D. Priftis, R. Farina and M. Tirrell, *Langmuir*, 2012, **28**, 8721–8729.

3   J. Sprakel, N. A. M. Besseling, F. A. M. Leermakers and M. A. Cohen Stuart, *Phys. Rev. Lett.*, 2007, **99**, 104504.

4   C. Schmitt and S. L. Turgeon, *Adv. Colloid Interface Sci.*, 2011, **167**, 63–70.

5   Y. Zhang, K. Han, D. Lu and Z. Liu, *Soft Matter*, 2013, **9**, 8723–8729.

6   D. Priftis, N. Laugel and M. Tirrell, *Langmuir*, 2012, **28**, 15947–15957.

7   S. Koga, D. S. Williams, A. W. Perriman and S. Mann, *Nat. Chem.*, 2011, **3**, 720–724.

8   E. Sokolova, E. Spruijt, M. M. K. Hansen, E. Dubuc, J. Groen, V. Chokkalingam, A. Piruska, H. A. Heus and W. T. S. Huck, *Proc. Natl. Acad. Sci.*, 2013, **110**, 11692–11697.

9   Z. Liu, Y. Jiao, Y. Wang, C. Zhou and Z. Zhang, *Adv. Drug Deliv. Rev.*, 2008, **60**, 1650–1662.

10 D. M. Pickup, R. J. Newport, E. R. Barney, J.-Y. Kim, S. P. Valappil and J. C. Knowles, *J. Biomater. Appl.*, 2014, **28**, 1226–1234.

11 Y. O. Popov, J. Lee and G. H. Fredrickson, *J. Polym. Sci. Part B Polym. Phys.*, 2007, **45**, 3223–3230.

12 Q. Wang and J. B. Schlenoff, *Macromolecules*, 2014, **47**, 3108–3116.

13 E. Spruijt, A. H. Westphal, J. W. Borst, M. A. Cohen Stuart and J. van der Gucht, *Macromolecules*, 2010, **43**, 6476–6484.

14 D. Priftis and M. Tirrell, *Soft Matter*, 2012, **8**, 9396–9405.

15 K. Abe, M. Koide and E. Tsuchida, *Polym. J.*, 1977, **9**, 73–78.

16 C. J. Ochs, G. K. Such, B. Städler and F. Caruso, *Biomacromolecules*, 2008, **9**, 3389–3396.

17 J. T. G. Overbeek and M. J. Voorn, *J. Cell. Comp. Physiol.*, 1957, **49**, 7–26.

18 E. Spruijt, J. Sprakel, M. Lemmers, M. A. C. Stuart and J. van der Gucht, *Phys. Rev. Lett.*, 2010, **105**, 208301.

19 S. L. Perry, Y. Li, D. Priftis, L. Leon and M. Tirrell, *Polymers*, 2014, **6**, 1756–1772.

20 E. Spruijt, S. A. van den Berg, M. A. Cohen Stuart and J. van der Gucht, *ACS Nano*, 2012, **6**, 5297–5303.

21 S. Rothemund, M. Beyermann, E. Krause, G. Krause, M. Bienert, R. S. Hodges, B. D. Sykes and F. D. Soennichsen, *Biochemistry (Mosc.)*, 1995, **34**, 12954–12962.

22 S. Y. Hong, J. E. Oh and K.-H. Lee, *Biochem. Pharmacol.*, 1999, **58**, 1775–1780.

23 A. M. Oelker, S. M. Morey, L. G. Griffith and P. T. Hammond, *Soft Matter*, 2012, **8**, 10887–10895.

24 S. L. Perry, L. Leon, K. Hoffmann, M. Kade, D. Priftis, Katie Black, Wong, Derek, Klein, Ryan, Pierce, Charles, K. Margossian, J. Whitmer, J. Qin, J. J. de Pablo and M. Tirrell, *Nature Communications. In press.*

25 J. van der Gucht, E. Spruijt, M. Lemmers and M. A. Cohen Stuart, *J. Colloid Interface Sci.*, 2011, **361**, 407–422.

26 D. Priftis, K. Megley, N. Laugel and M. Tirrell, *J. Colloid Interface Sci.*, 2013, **398**, 39–50.

27 C. G. de Kruif, F. Weinbreck and R. de Vries, *Curr. Opin. Colloid Interface Sci.*, 2004, **9**, 340–349.

28 L. Wang, R. A. Friesner and B. J. Berne, *J. Phys. Chem. B*, 2011, **115**, 9431–9438.

29 Y. Li and Q. Huang, *J. Phys. Chem. B*, 2013, **117**, 2615–2624.

30 W. G. Hoover, *Phys. Rev. A*, 1985, **31**, 1695–1697.

31 P. Bjelkmar, P. Larsson, M. A. Cuendet, B. Hess and E. Lindahl, *J. Chem. Theory Comput.*, 2010, **6**, 459–466.

32 S. Piana, K. Lindorff-Larsen and D. E. Shaw, *Biophys. J.*, 2011, **100**, L47–L49.

33 K. Lindorff-Larsen, P. Maragakis, S. Piana, M. P. Eastwood, R. O. Dror and D. E. Shaw, *PLoS ONE*, 2012, **7**, e32131.

34 A. Savelyev and G. A. Papoian, *J. Am. Chem. Soc.*, 2006, **128**, 14506–14518.

35 I. S. Joung and Thomas E. Cheatham, *J. Phys. Chem. B*, 2008, **112**, 9020–9041.

36 B. Hess, C. Kutzner, D. van der Spoel and E. Lindahl, *J. Chem. Theory Comput.*, 2008, **4**, 435–447.

37 M. Parrinello and A. Rahman, *J. Appl. Phys.*, 1981, **52**, 7182 –7190.

38 T. Darden, D. York and L. Pedersen, *J. Chem. Phys.*, 1993, **98**, 10089–10092.

39 B. Hess, H. Bekker, H. Berendsen and J. Fraaije, *J. Comput. Chem.*, 1997, **18**, 1463–1472.

40 A. Erbaş, D. Horinek and R. R. Netz, *J. Am. Chem. Soc.*, 2012, **134**, 623–630.

41 Q. Yan and J. J. de Pablo, *J. Chem. Phys.*, 1999, **111**, 9509–9516.

42 N. Rathore, T. A. Knotts and J. J. de Pablo, *Biophys. J.*, 2003, **85**, 3963–3968.

43 N. Rathore, M. Chopra and J. J. de Pablo, *J. Chem. Phys.*, 2005, **122**, 024111.

44 D. J. Earl and M. W. Deem, *Phys. Chem. Chem. Phys. PCCP*, 2005, **7**, 3910–3916.

45 R. P. R. Nanga, J. R. Brender, J. Xu, G. Veglia and A. Ramamoorthy, *Biochemistry (Mosc.)*, 2008, **47**, 12689–12697.

46 P. Liu, B. Kim, R. A. Friesner and B. J. Berne, *Proc. Natl. Acad. Sci. U. S. A.*, 2005, **102**, 13749–13754.

47 H. G. Katzgraber, S. Trebst, D. A. Huse and M. Troyer, *J. Stat. Mech. Theory Exp.*, 2006, P03018.

48 G. Bussi, *Mol. Phys.*, 2014, **112**, 379–384.

49 M. Bonomi, D. Branduardi, G. Bussi, C. Camilloni, D. Provasi, P. Raiteri, D. Donadio, F. Marinelli, F. Pietrucci, R. A. Broglia and M. Parrinello, *Comput. Phys. Commun.*, 2009, **180**, 1961–1972.

50 W. Kabsch and C. Sander, *Biopolymers*, 1983, **22**, 2577–2637.

51 W. Humphrey, A. Dalke and K. Schulten, *J. Mol. Graph.*, 1996, **14**, 33–38.

52 C. R. Baiz, D. Schach and A. Tokmakoff, *Opt. Express*, 2014, **22**, 18724–18735.

53 A.-S. Yang and B. Honig, *J. Mol. Biol.*, 1995, **252**, 366–376.

54 M. Auton, L. M. F. Holthauzen and D. W. Bolen, *Proc. Natl. Acad. Sci.*, 2007, **104**, 15317–15322.

Figures
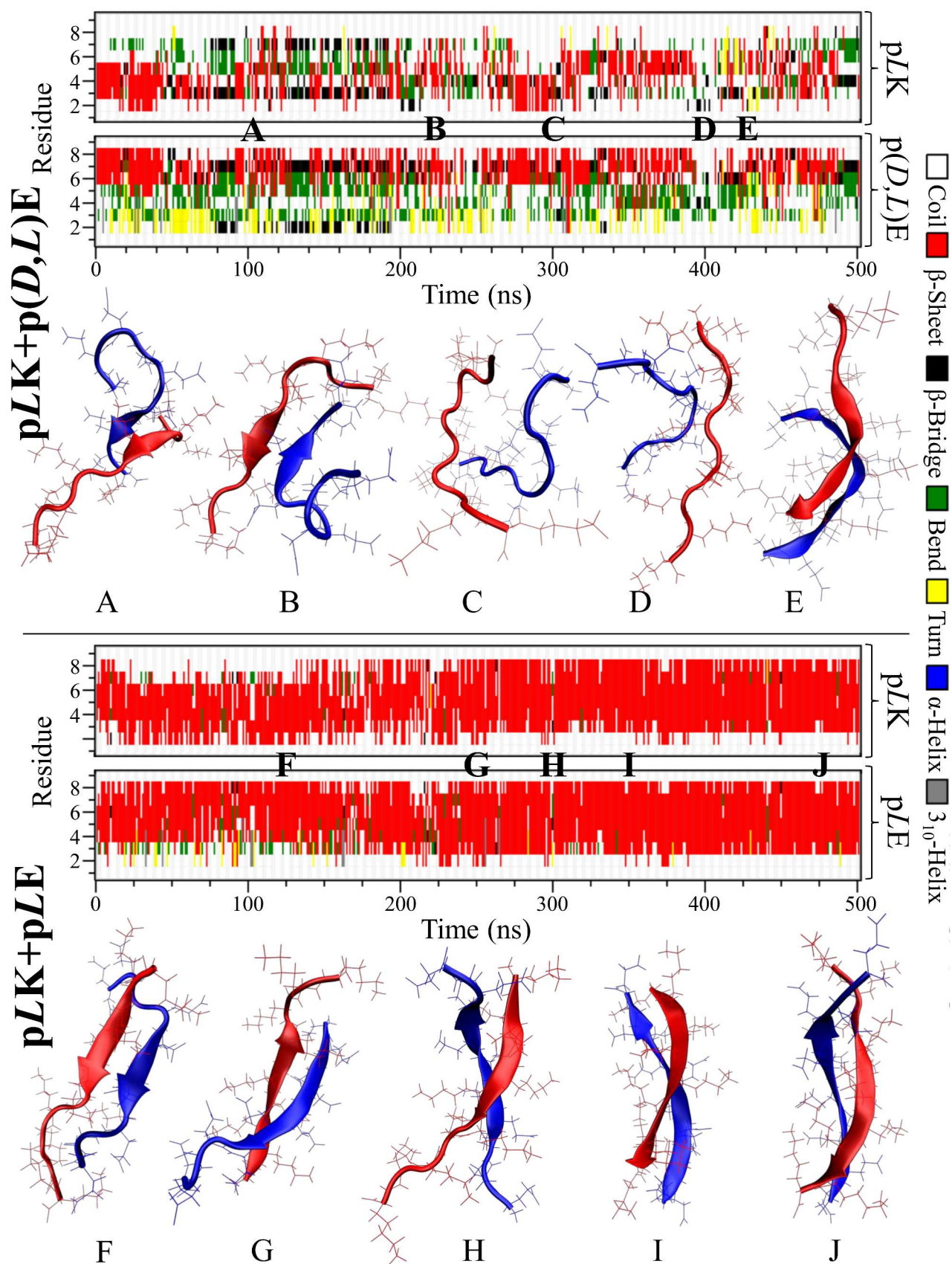
Figure 1. Secondary structure vs. time for REST2 simulations for pLK+p(D,L)E and pLK+pLE. Conformations at selected points in time are shown below each secondary structure plot at the time each letter is placed.
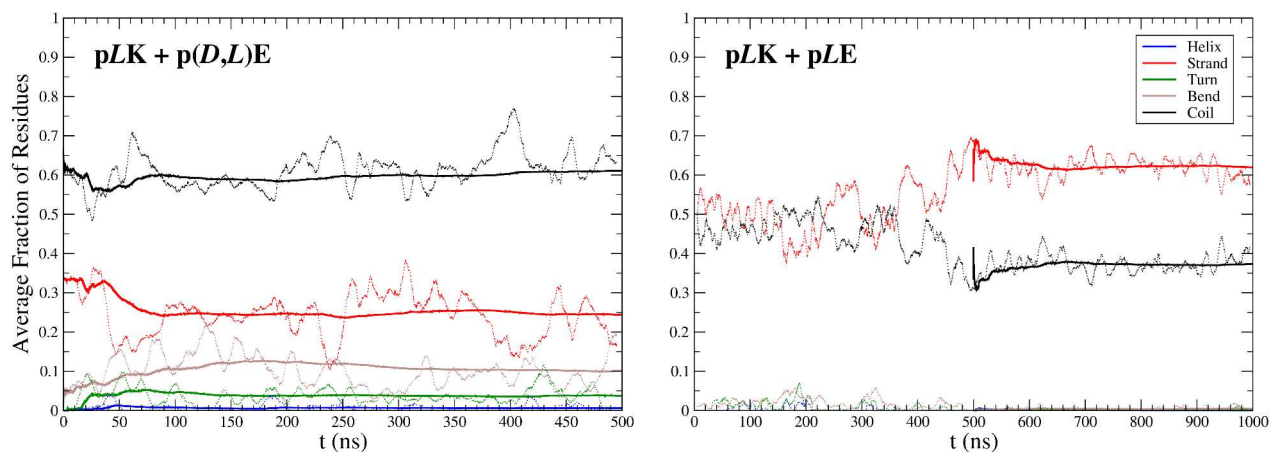
Figure 2. Average secondary structure versus time during the REST2 simulations of pLK+p(D,L)E and pLK+pLE. The thin, dotted line shows the running average over 10 ns, while the thick, solid line shows the total average starting from the beginning of convergence. The helix fraction is the sum of the α-helix and 3-helix fractions; likewise, the strand fraction is the sum of the β-sheet and β-bridge fractions.
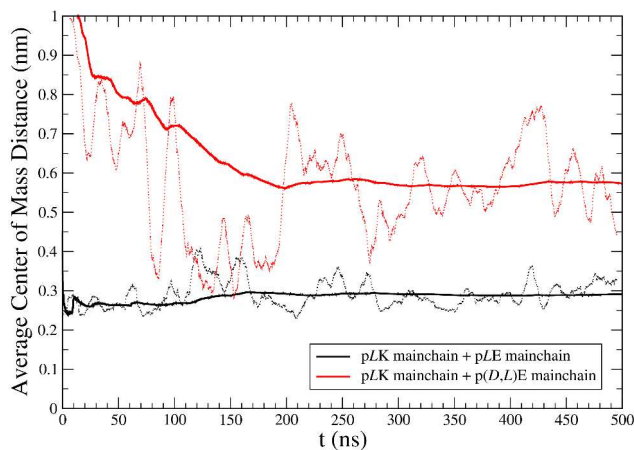
Figure 3. Average center of mass distance between Poly(glutamate) and Poly(lysine) for pLK+p(D,L)E and pLK+pLE. The thin, dotted line shows the running average over 10 ns, while the thick, solid line shows the total average. The average center of mass distance from the pLK+p(D,L)E system is shown in red, while the average from the pLK+pLE simulation is shown in black.
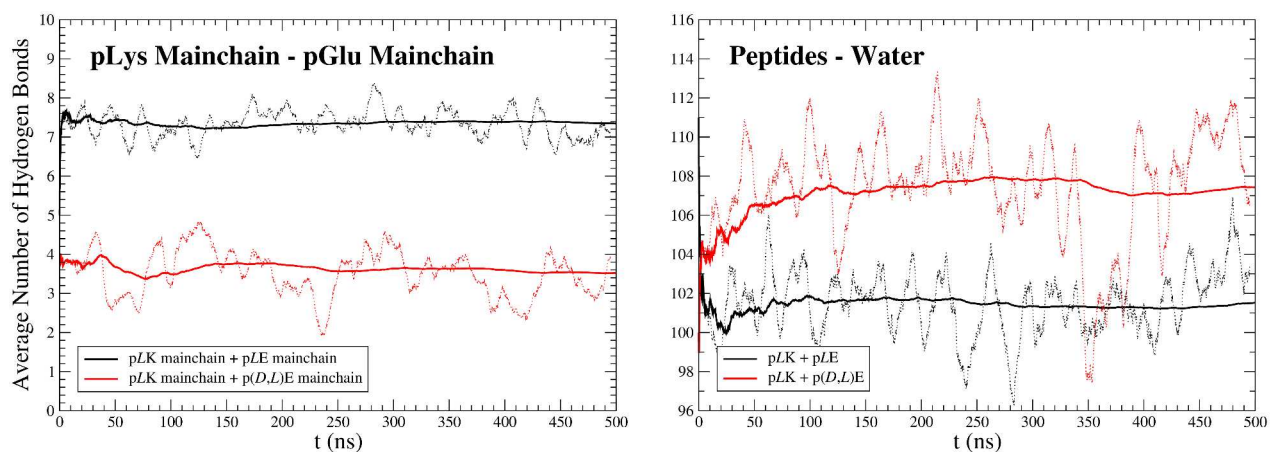
Figure 4. Average predicted number of hydrogen bonds versus time for pLK+p(D,L)E and pLK+pLE between PGlu and PLys, and between PGlu and water. The thin, dotted line shows the running average over 10 ns, while the thick, solid line shows the total average. The average number of hydrogen bonds between the poly(glutamatic acid) and poly(lysine) strands is shown in the left figure, while the average number of hydrogen bonds between the peptides and water is shown in the right hand figure. The average number of hydrogen bonds from the pLK+p(D,L)E system is shown in red, while average from the pLK+pLE is shown in black.
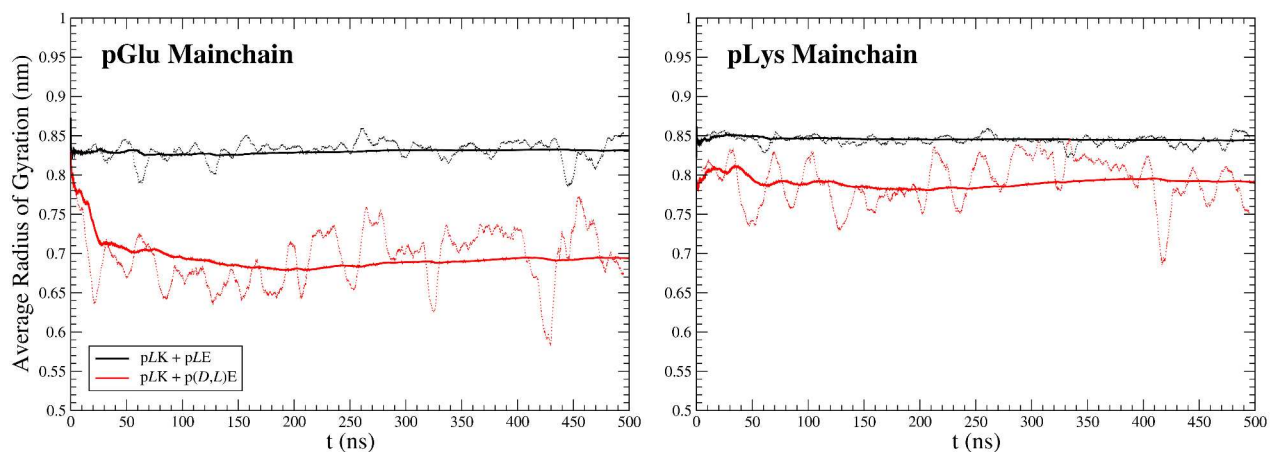
Figure 5. Average predicted radius of gyration versus time for the main chains of PGlu and PLys for p*L*K+p(*D,L*)E and p*L*K+p*L*E. The thin, dotted lines show the local, running average over 10 ns. The thick, solid line shows the total average. The average radius of gyration for the poly(glutamatic acid) strand is shown in the left figure, while the average radius of gyration of Poly(lysine) is shown in the right hand figure. The average radius of gyration of the peptide from the p*L*K+p(*D,L*)E system is shown in red, while the average from the p*L*K+p*L*E system is shown in black.
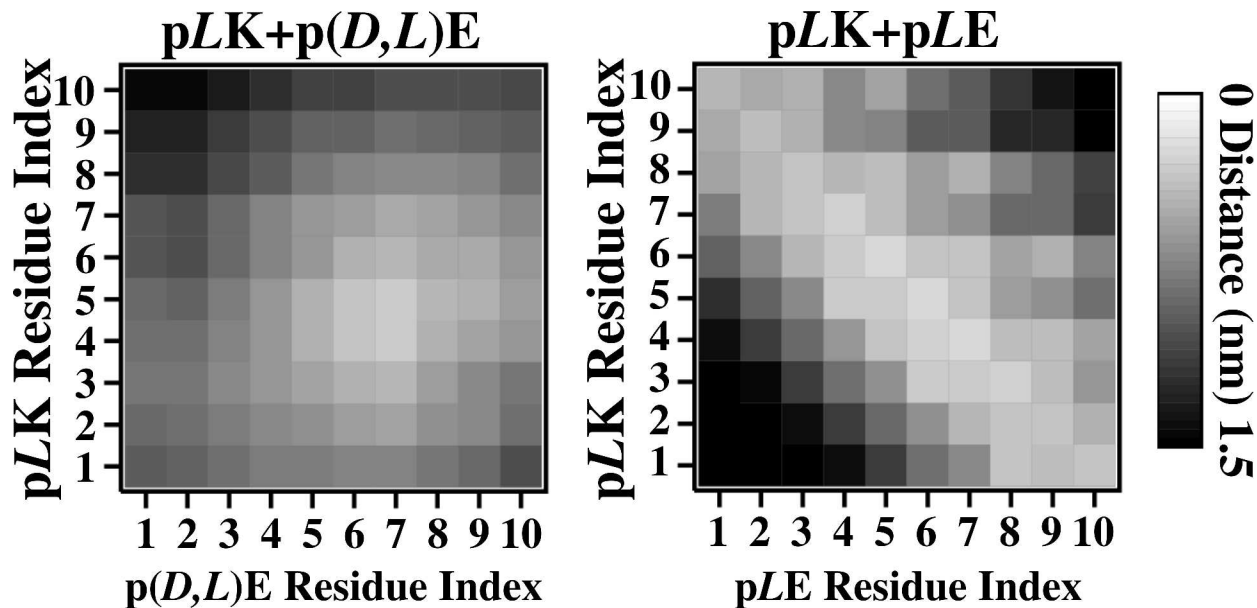
Figure 6. Contact maps of p*L*K+p(*D,L*)E (left) and p*L*K+p*L*E (right) for the REST2 simulations. The average minimum distance between each pair of residues over the last 500 ns is shown varying from white (0 nm) to black (≥ 1.5 nm).
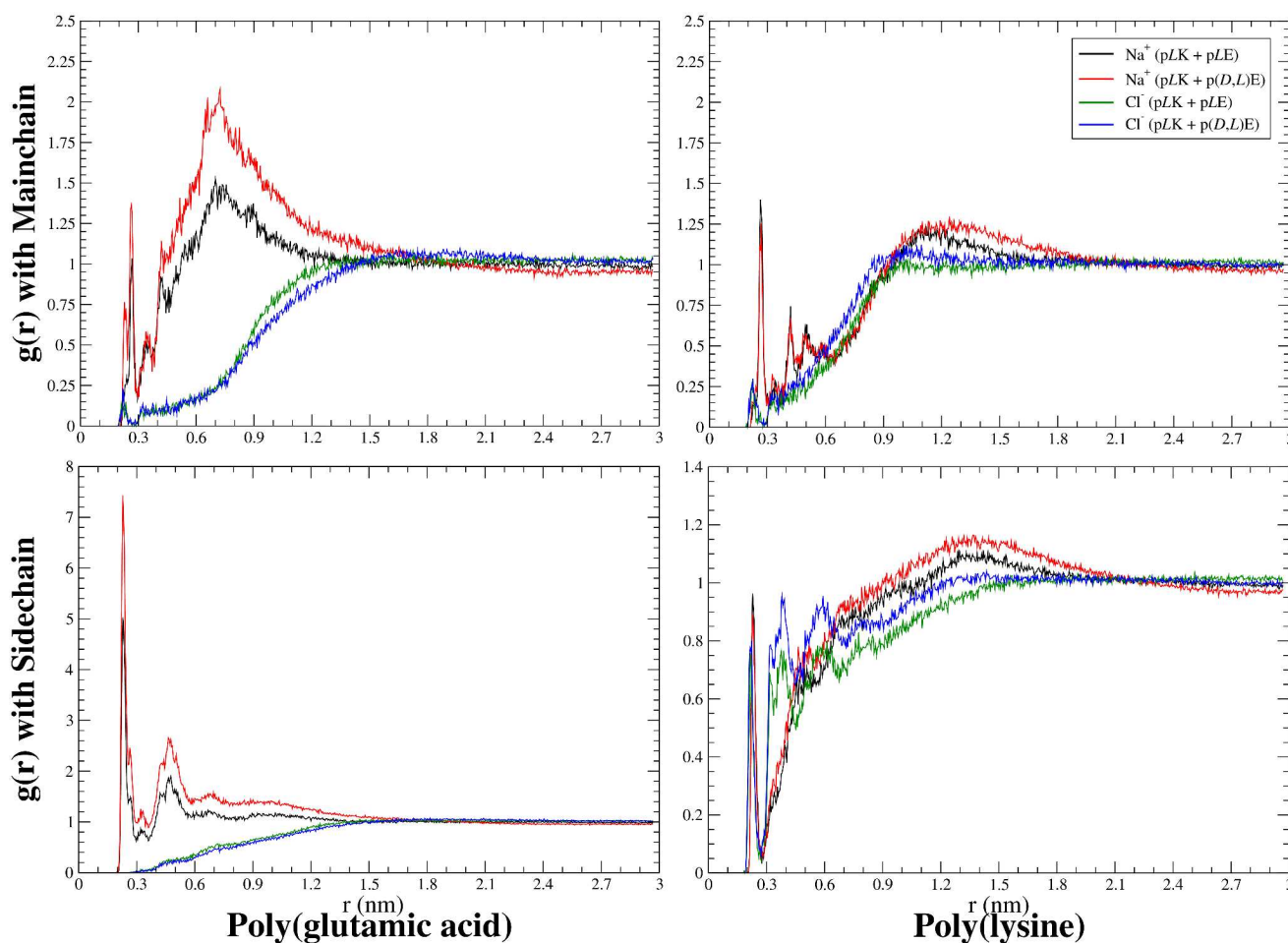
Figure 7. Radial distribution functions for Na⁺ and Cl⁻ ions with the main chains and side chains of PGlu and PLys. The plots on the left are shown for the rdf with parts of poly(glutamic acid) chain. On the right, the plots correspond to rdf with the poly(lysine) chain. The top figures show the rdf of the ions with the main chain of the peptide. The bottom figures show the rdf with the side chains. In all plots, for pLK+pLE, the rdf of Na⁺ is shown in black and Cl⁻ is shown in green. For pLK+p(D,L)E, the rdf of Na⁺ is shown in red and Cl⁻ is shown in blue.
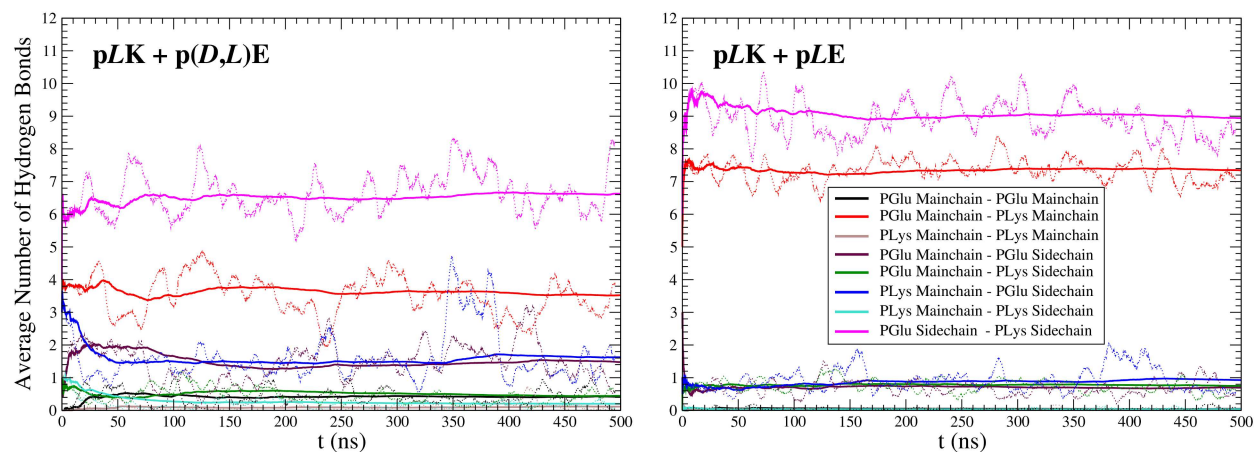
Figure 8. Hydrogen bonding between different regions of the peptides. The thick lines show the overall average while the dotted lines show the local, running average over 10 ns.
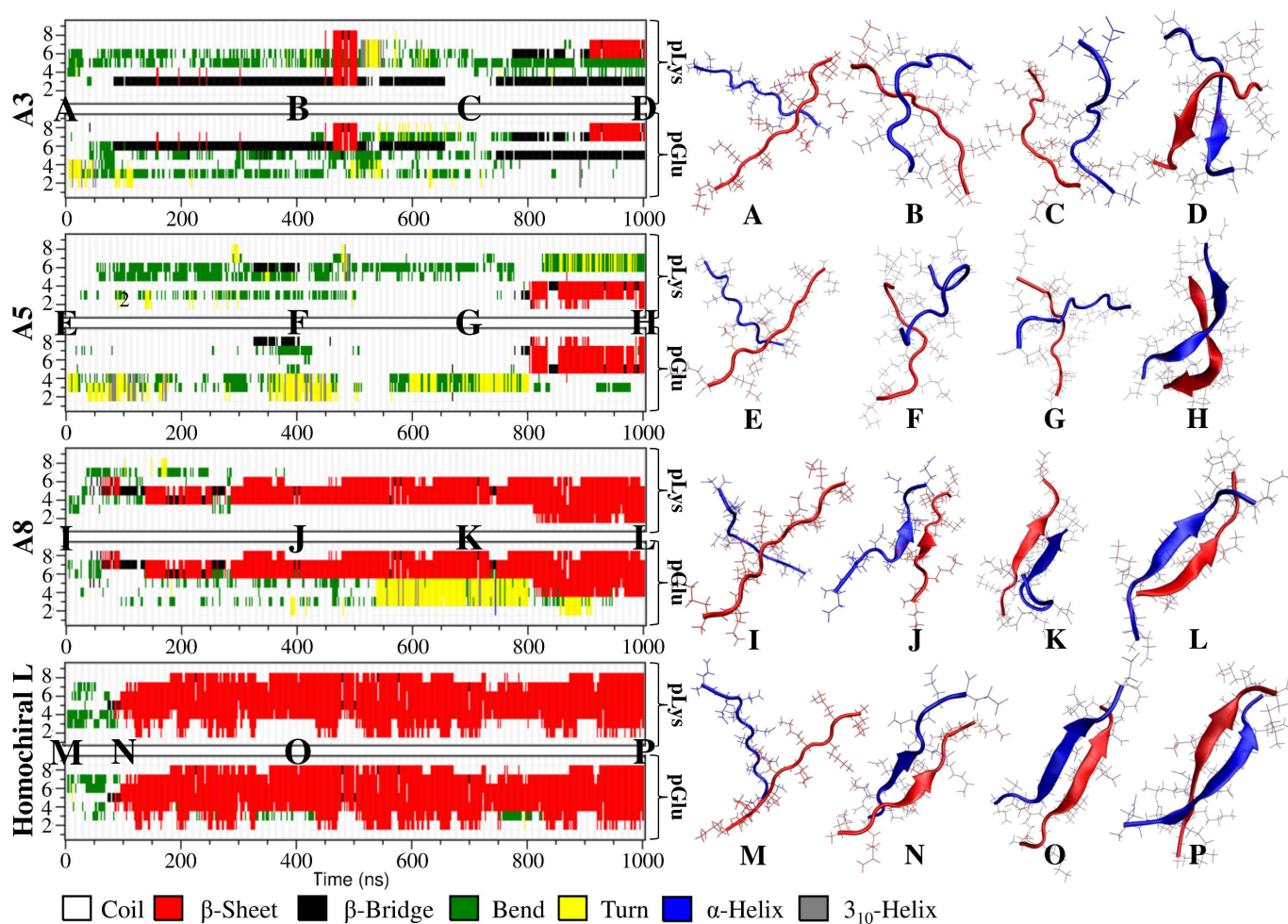
Figure 9. Secondary structure of each residue vs. time for various MD simulations of polypeptide pairs. "A" denotes a non-homochiral sequence. These sequences are given in Table 1. The PGlu chains are the bottom half of each figure, while the PLys chains are in the top half. At each time, the secondary structure of each residue along the y-axis is denoted by the color. For example, red indicates a β-sheet structure. The structures of PLys and PGlu are shown at 0, 400, 700, and 1000 ns for each pair. PLys is shown in red, and PGlu is shown in blue.
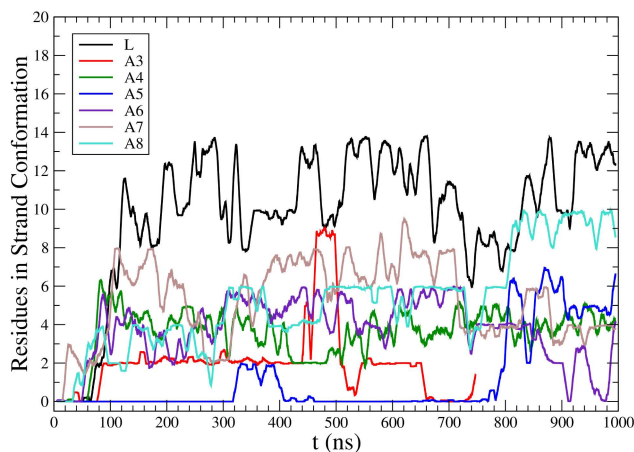
Figure 10. Average number of residues in strand conformation (β-sheet or β-bridge) vs. time for each pair of peptides.
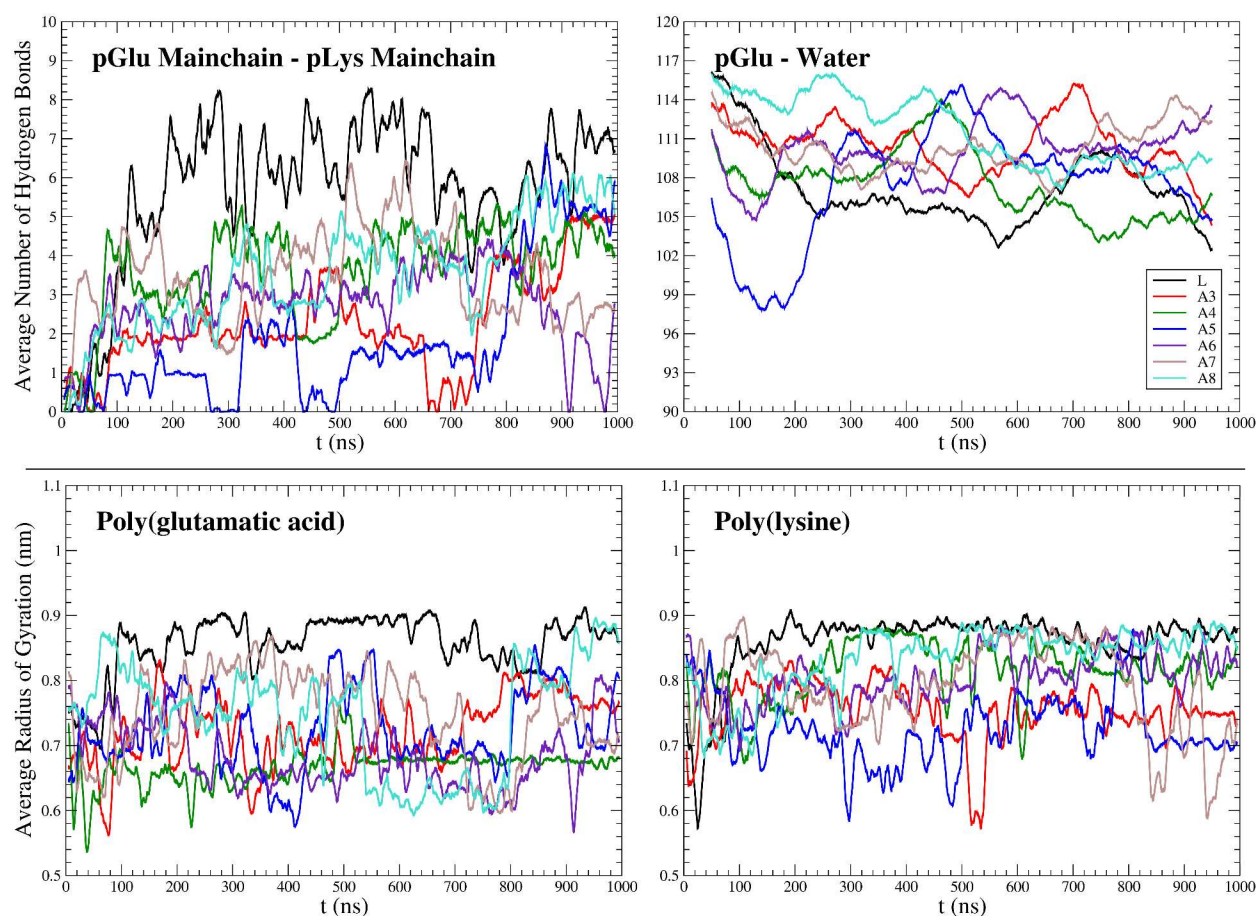
Figure 11. Running average of the number of hydrogen-bonds between the PGlu and PLys mainchains over 10 ns, and between the peptides and water over 100 ns for various combinations of PLys and PGlu with different chiralities (Top). 10 ns running average of the radius of gyration over 10 ns for poly(glutamic acid) and poly(lysine) vs. time for various chiral sequences of poly(glutamic acid) with poly(*L*-lysine) (Bottom).
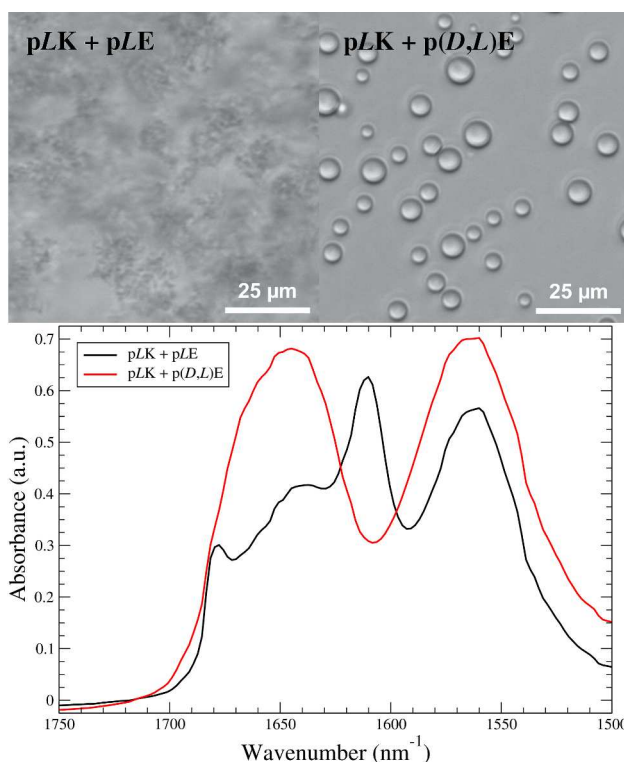
Figure 12. Brightfield optical micrographs showing the (a) solid precipitates resulting from the stoichiometric electrostatic complexation of pLK+pLE, or the (b) liquid coacervates resulting from the complexation of pLK+p(D,L)E at a total residue concentration of 6 mM and 100 mM NaCl. (c) FTIR spectra showing the amide I region for both a solid precipitate (blue) and a liquid coacervate (black). Samples were prepared in D2O at a concentration of 9.5 mM with respect to monomer and 100 mM NaCl, and centrifuged prior to use. Both materials show a peak around 1642-1646 cm-1, characteristic of random coil polypeptide structure, and a peak at 1563 cm-1 corresponding to the carbonyl stretching of the glutamic acid side chain. The precipitate sample also shows characteristic peaks at 1610 cm-1 and 1678 cm-1, typical of an aggregated beta strand structure. All samples were prepared using polypeptides with an average N = 100.
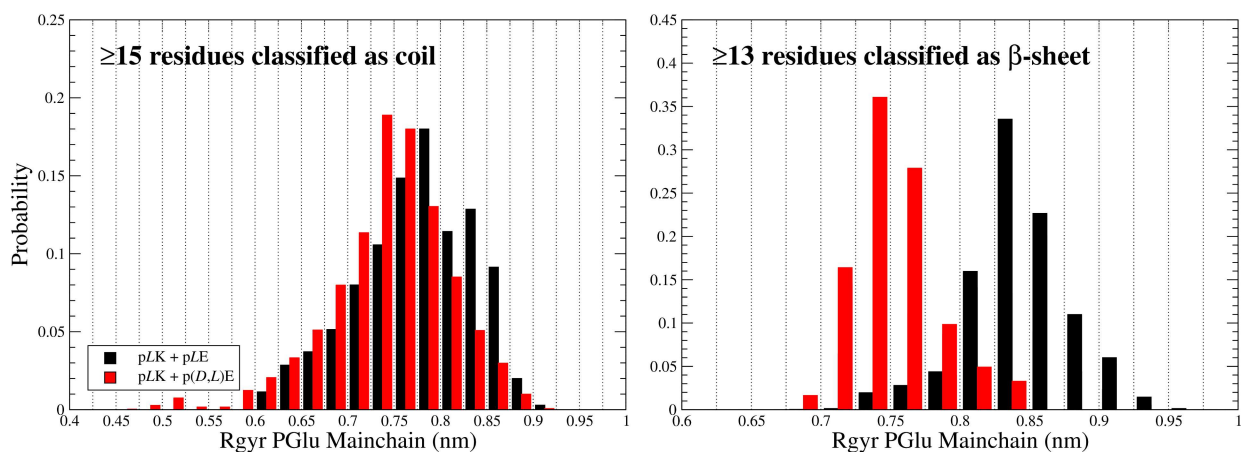

Figure 13. Histograms of the radius of gyration of Poly(glutamic acid). The distribution for structures with at least 15 residues classified as coil is shown on the left, while the distribution for structures with at least 13 residues in a β-sheet is shown on the right. The fraction of states with a radius of gyration in that bin is shown in black for the pLK+pLE system, and red for the pLK+p(D,L)E system.
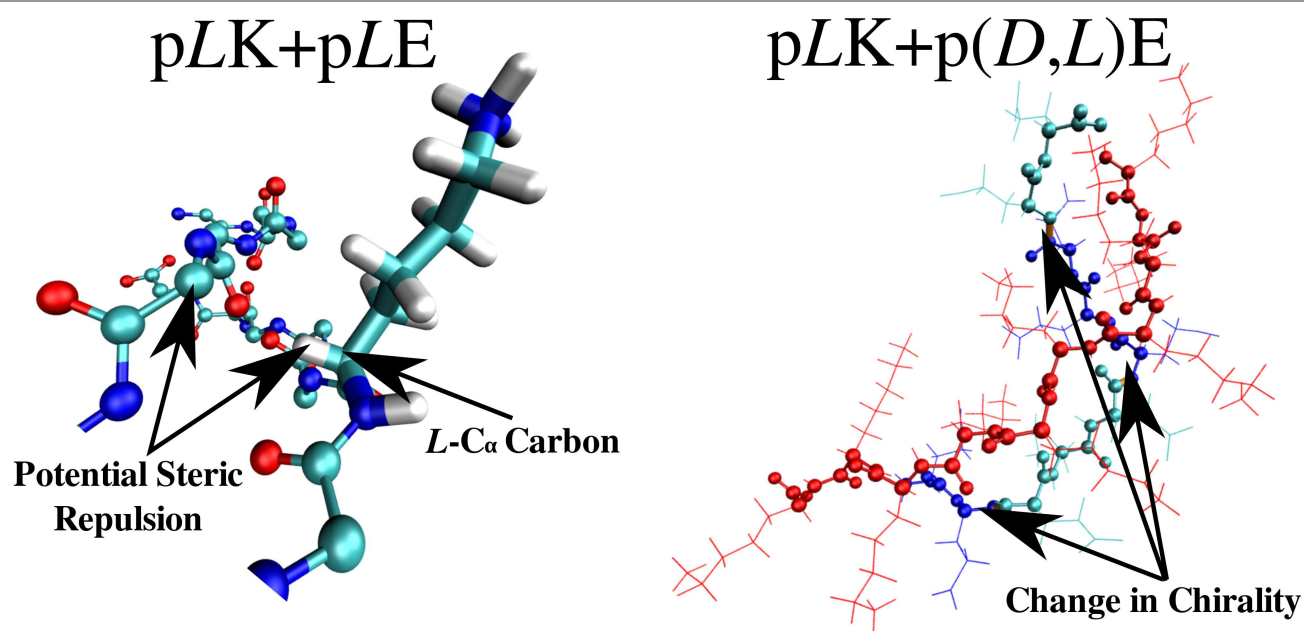
Figure 14. Structure of the anti-parallel β-sheet backbones formed by pLK+pLE and the potential steric repulsions if an *L*-Glu was changed to a *D*-Glu (left), and the kinks formed by the structure of pLK+p(*D,L*)E with the most β-sheets in order to avoid these repulsions (right). In left-hand figure, carbons are shown in cyan, nitrogens in blue, oxygens in red, and hydrogens in white. The structure is the anti-parallel β-sheet formed at 1000 ns by pLK+pLE. In the right-hand figure, the poly(lysine) chain is shown in red, while the *L*-Glu residues are shown in dark blue and the *D*-Glu residues are shown in cyan. The structure shown is the one formed at 266.23 ns by pLK+p(*D,L*)E where 14 residues are counted by DSSP as being in a β-sheet.